Engineering Structures 183 (2019) 94–109

Contents lists available at ScienceDirect

Engineering Structures

journal homepage: www.elsevier.com/locate/engstruct

Structural performance of CFRP-strengthened concrete-filled stainless steel tubular short columns

Alfarabi M. Sharif, Galal M. Al-Mekhlafi, Mohammed A. Al-Osta*

Department of Civil Engineering, King Fahd University of Petroleum & Minerals, Dhahran 31261, Saudi Arabia

ARTICLE INFO

Keywords:
Stainless steel
Concrete-filled stainless steel tubes
Carbon fiber reinforced polymer
Experimental work
Finite element analysis
Analytical model

ABSTRACT

The use of concrete-filled stainless steel tubular (CFSST) members is relatively innovative and new. CFSST columns can be used for bridge piers, multi-story buildings and other supporting structures. However, a common mode of failure with these type of tubular composite columns is inelastic outward local buckling occurring at the column ends. Therefore, this paper presents the results of experimental, numerical and analytical investigations into the behavior of circular CFSST columns strengthened by carbon fiber reinforced polymer (CFRP) wrap and subjected to axial compression loading. The experimental investigation comprised three series of tests. The main variables tested were the diameter to thickness ratio of the stainless steel tube and the thickness of the CFRP wrap. 3D finite element models (FEMs) were developed for CFRP-wrapped CFSST columns using the ABAQUS software and were validated with experimental results. An extensive parametric study was carried out by using the validated FEMs. It was shown from the experimental and FEMs results that CFRP jacketing was highly effective in improving the axial load carrying capacity and axial shortening capacity of the CFSST columns. Finally, an analytical model based on the FE parametric study results was proposed to predict the axial load carrying capacity of the CFRP-wrapped CFSST columns.

1. Introduction

Recently, stainless steel material has been used as a construction material, while it was previously only used for special purposes or for decoration due to its advantages over carbon steel which include its aesthetic appearance, high resistance to corrosion, ease of maintenance and high fire resistance. Taking into account the long-term cost, stainless steel material can be selected as a competitive material [1]. In addition, one of the reasons for considering stainless steel as a competitive structural material is its favorable mechanical properties and its high ductility. Stainless steel material exhibits a nonlinear stress- strain relationship with no defined yield point, unlike carbon steel material [2].

Many investigations have been conducted into the structural behavior of unfilled (hollow) stainless steel sections. Important early reported studies exploring the structural performance of hollow stainless steel sections were performed by Rasmussen and Hancock [3]. Subsequently, a series of studies has been performed to understand more about these tubular sections [4–7]. These studies have contributed greatly to the expansion of information on the structural performance of stainless steel elements and, at the same time, have highlighted some shortcomings in the existing design standards such as American stainless steel design specifications SEI/ASCE-8 and EN 1993-1-4. For the sake of simplification, these existing design standards disregarded some mechanical characteristics observed in stainless steel, such as strong strain hardening and the rounded stress-strain relationship. This simplification method, adopted in the existing standard codes, includes using an elastic perfectly plastic bilinear material model that leads to a significant degree of conservatism. A new, efficient and more rational method has been developed to consider the particular stress-strain characteristics of stainless steel [8–10]. Instead of considering that the maximum design stress limit is the 2% proof stress, as in the existing standards, a new method called the continuous strength method (CSM) [11–16] has been developed as a deformation-based design method to exploit the noticeable strain hardening in the determination of stainless steel cross-section resistances. However, the initial high cost of stainless steel material has limited the extensive use of stainless steel material in structural construction. Hence, concrete-filled stainless steel tube (CFSST) columns have been developed to balance the high initial stainless steel material cost, as well as to enhance the structural behavior.

CFSST columns are composite structural elements composed of stainless steel and concrete. Using CFSST columns leads to savings in column size compared with traditional metallic or concrete

* Corresponding author.
E-mail address: malosta@kfupm.edu.sa (M.A. Al-Osta).

https://doi.org/10.1016/j.engstruct.2019.01.011
Received 12 August 2018; Received in revised form 2 January 2019; Accepted 2 January 2019

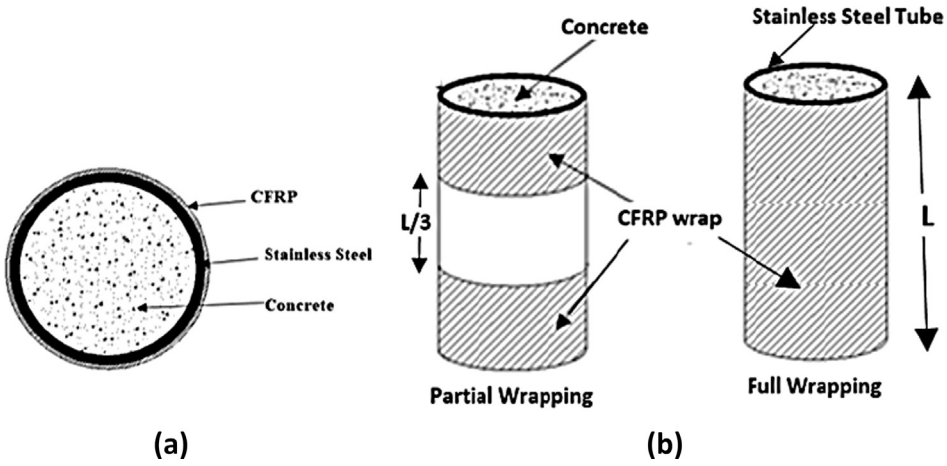

Fig. 1. CFRP-wrapped CFSST scheme (a) Cross Section (b) CFRP arrangement.

constructions, which ultimately leads to financial savings. The use of stainless steel tubes filled with concrete is comparatively new and innovative, and not only offers the advantages mentioned above, but also the durability that stainless steel provides [17]. Extensive investigations were conducted to understand the structural performance of concrete-filled carbon steel tubular (CFCST) columns [18–23] and CFSST columns [17,24–31]. These studies indicated that the structural performance of these composite structures is superior to steel or concrete structures since the composite action plays a mutually beneficial role where the steel tube confines the concrete core and the concrete core postpones the occurrence of local buckling in the steel tube. It is clear from these studies [17–30] that the common mode of failure of these composite structures is the outward local buckling of steel tubes which leads to degradation in strength and ductility due to excess inelastic deformation. Therefore, to strengthen the concrete-filled tubes against further loads, outward local buckling has to be postponed or even suppressed.

Recently, a new alternative technique was developed to strengthen concrete-filled steel tubes by gluing the Glass fiber-reinforced polymer (GFRP) or carbon fiber-reinforced polymer (CFRP) to the outer surface of steel tubes. The use of CFRP and GFRP to strengthen civil infrastructure was developed due to their highly desirable material properties such as high tensile strength, ease of fabrication, light weight and excellent corrosion resistance. An investigation was conducted experimentally and mathematically into the performance of CFRP to strengthen CFCST columns by Ding et al. [32]. As confirmed by the test results for axial compression loading and seismic loading, CFCST reinforced with CFRP can lead to improved seismic performance as reported by Xiao et al. [33]. An increase in strength and ductility due to using GFRP to reinforce CFCST columns was reported by Hu et al. [34] and Yu et al. [35]. Experimental investigations to study the performance of CFRP composite bonded circular CFCST subjected to axial compression were conducted by Haedir & Zhao [36] and Sundarraja & Prabhu [37]. The experimental results showed that improvement in the axial capacity is possible by CFRP. Feng et al. [38] carried out a study to investigate the flexural performance of CFRP-confined CFSST beams. Dong et al. [39] and Prabhu et al. [40] studied the performance of CFRP-partially wrapped CFCST columns. They concluded that partial wrapping is less effective than full wrapping in terms of the load carrying capacity.

It should be noted from the literature that the above-mentioned studies were all conducted on CFCSTs. To the best knowledge of the authors, the structural behavior of CFRP confined CFSST columns under axial loading has not yet been investigated. The use of CFRP wrap with stainless steel tubular columns is intended for strengthening structurally deficient existing columns rather than newly constructed ones. Therefore, the main objective of this paper is to investigate the behavior and strength of axially compressive loaded CFRP wrapped circular CFSST columns using experimental tests followed by finite element study. Finite element models (FEMs) were first validated by experimental results. Based on the validated FEMs, a series of parametric studies was carried out. The experimental and numerical results were employed to develop an analytical model to predict the load carrying capacity of CFRP-confined circular CFSST short columns under axial loading.

2. Experimental investigation

The experimental work was conducted to study the structural performance of CFRP-confined circular CFSST columns under axial compression loading by using three cross-section sizes. The experimental work involves different tests, such as stainless steel material tensile coupon, concrete uniaxial compressive, and thirteen stub column tests under axial loading. The preparation of the experimental specimens and test setup used for the experimental work is described and reported in the following sections.

2.1. Test specimens

The experimental program was designed and performed to evaluate the structural performance of CFRP wrapped CFSST columns under axial monotonic compressive loading. Fig. 1a shows a cross-section of CFRP-confined CFSST columns. Experiments were conducted on three different circular hollow stainless steel (CHSS) cross-sectional sizes: CHSS 101 × 2, CHSS 114 × 3 and CHSS 101 × 1.5, where the first number refers to the tube's outer diameter and the second number represents the tube thickness. For each section size, four stub column tests were carried out, one of them without CFRP and the other three with CFRP. Normal concrete was used. The main variable parameters in the tests were the stainless steel outer diameter to thickness ratio (D/t_s) and the CFRP jacket thickness (t_f). All of the stub columns were 290 mm in length for two reasons: first to ensure that the specimens are suitably short to avoid overall flexural buckling, while the second reason relates to the available height in the hydraulic testing machine. The test specimens and parameters are summarized in Table 1. The CFRP arrangement was full wrapping, except one specimen that was a partial arrangement, as displayed in Fig. 1b. In the partially wrapped specimen, two-thirds of the length were confined by CFRP wrapping. The middle third was free from CFRP wrapping. This partial wrapping is limited to a diameter to thickness ratio of 50; it was used only in the experimental program as a control to compare with the full wrap one. It was not included in the numerical and mathematical parts later.

Table 1
Measured geometric dimensions and test variables of CFSST.

Series	Specimen label	Stainless steel tube			CFRP		
		D (mm)	t_s (mm)	D/t_s	No. of plies	t_f (mm)	Arrangement
G1	C0-37	114.3	3.05	37.5	0	0	–
	C1-37	114.3	3.05	37.5	1	0.29	Full wrapping
	C2-37	114.3	3.05	37.5	2	0.58	Full wrapping
	C3-37	114.3	3.05	37.5	3	0.87	Full wrapping
G2	C0-50	101	2	50.1	0	0	–
	C1-50	101	2	50.1	1	0.29	Full wrapping
	C2-50	101	2	50.1	2	0.58	Full wrapping
	C3-50	101	2	50.1	3	0.87	Full wrapping
G3	C0-67	101	1.5	67.3	0	0	–
	C1-67	101	1.5	67.3	1	0.29	Full wrapping
	C2-67	101	1.5	67.3	2	0.58	Full wrapping
	C3-67	101	1.5	67.3	3	0.87	Full wrapping
G4	C2-50-partial	101	2	50.1	2	0.58	Partial wrapping

Each specimen was given a distinctive label starting with the letter C followed by a number referring to the number of CFRP plies. The letter C stands for the CFSST columns. The second number represents the D/t_s ratio. For example, the label C2-37 refers to a CFSST column that has a D/t_s ratio of 37.5 and is wrapped by two CFRP plies, respectively.

2.2. Material properties

2.2.1. Stainless steel

2.2.1.1. Chemical composition analysis. Like carbon steel material, stainless steel material has various grades due to variations in its chemical composition as well as heat treatment. Five main groups are available to classify stainless steel material regarding its metallurgical structure. These five groups are namely austenitic, ferritic, duplex, matensitic and precipitation hardening. In this study, a chemical composition analysis was carried out in a material science laboratory to identify the stainless steel material used in test specimens. The chemical composition analysis was conducted on three small samples taken from the CHSSTs. From the chemical analysis of the test specimens shown in Table 2, the stainless steel material used in this study was austenitic stainless steel Grade 304.

2.2.1.2. Mechanical properties. To determine the material stress-strain relationship of the tested stainless steel material, tensile coupon experiments were conducted. Two longitudinal coupons for each cross-section were extracted at 90° from the weld location to obtain the average bending residual stresses formed due to the cold-rolling process, as illustrated in Fig. 2. Both ends of the tensile coupon were flattened in order to be gripped by the test machine. For the three cross-sections, six tensile coupons were tested according to the requirements of ASTM E8M [41]. The obtained stress-strain curves of the tested tensile coupons are shown in Fig. 3, where the stainless steel material displays a curved stress-strain relationship with no specific yield stress point. Commonly, the stress-strain relationship of stainless steel can be

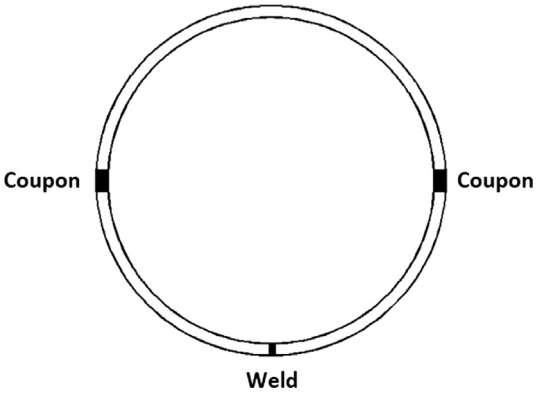

Fig. 2. Tensile coupon locations.

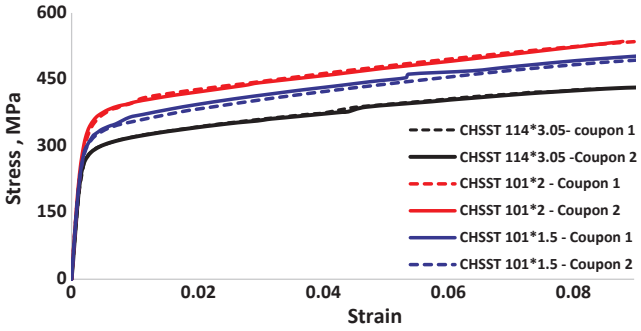

Fig. 3. Stress-strain curves for CHSSTs material.

represented by the Ramberg-Osgood model [42] modified by Hill [43] as illustrated in Table 3, where: E_0, $E_{0.2}$, ν, $\sigma_{0.2}$ and $\sigma_{1.0}$ are, respectively, the initial elastic modulus, the elastic modulus at 0.2% proof stress, Poisson's ratio, 0.2% proof stress and 1.0% proof stress. The coefficients (n) and ($n_{0.2,1}$) are strain-hardening exponents determined from the stress-strain curves fitting.

2.2.2. Normal concrete

The concrete material was cast by using local commercial constituents that were available to produce normal concrete with typical mixing and curing techniques, and the mix ratio was 1:2.1:3.1 by weight. After several initial trials, one concrete mix was chosen to obtain the appropriate strength using ordinary Portland cement. The compressive strengths (f_c') of concrete were determined by testing cylindrical specimens in accordance with ASTM C39 [44] with a dimension of 75 × 150 mm. The average of six cylinders tested for each batch was taken as the applicable value of f_c' for that batch. The average of f_c' at 28 days was determined as 43.6 MPa with a standard deviation (SD) and a coefficient of variation (COV), respectively, which were 1.14 and 0.026.

2.2.3. CFRP material

The mechanical properties of unidirectional carbon fiber material with a thickness of 0.29 mm per ply and adhesive were taken from the manufacturer's manual. The modulus of elasticity and the ultimate tensile strength in the fiber direction are, respectively, 220 GPa and

Table 2
Chemical compositions (% by weight) of test material.

Specimens	Fe (%)	Cr (%)	Ni (%)	C (%)	Si (%)	Mn (%)	Nb (%)	P (%)	S (%)	Mo (%)
1	71.7	18.96	7.8	0.0452	0.284	0.0048	< 0.0040	< 0.0005	< 0.0005	0.115
2	71.7	18.51	7.9	0.0477	0.531	0.004	< 0.0040	< 0.0005	< 0.0005	0.101
3	70.0	18.71	7.7	0.0212	0.445	1.81	< 0.0040	< 0.0005	< 0.0005	0.328

Table 3
Average measured tensile material properties used in the Ramberg-Osgood model.

Specimen	E0 (MPa)	ν	E0.2 (MPa)	σ 0.2 (MPa)	σ 1.0 (MPa)	Ramberge–Osgood coefficients	
						n	$n_{0.2,1}$
CHSST 114 × 3	189,099	0.33	13,611	293	332	10	1.91
CHSST 101 × 2	208,228	0.33	17,747	357	401	9.21	1.89
CHSST 101 × 1.5	204,581	0.30	16,285	322	365	9.09	1.69

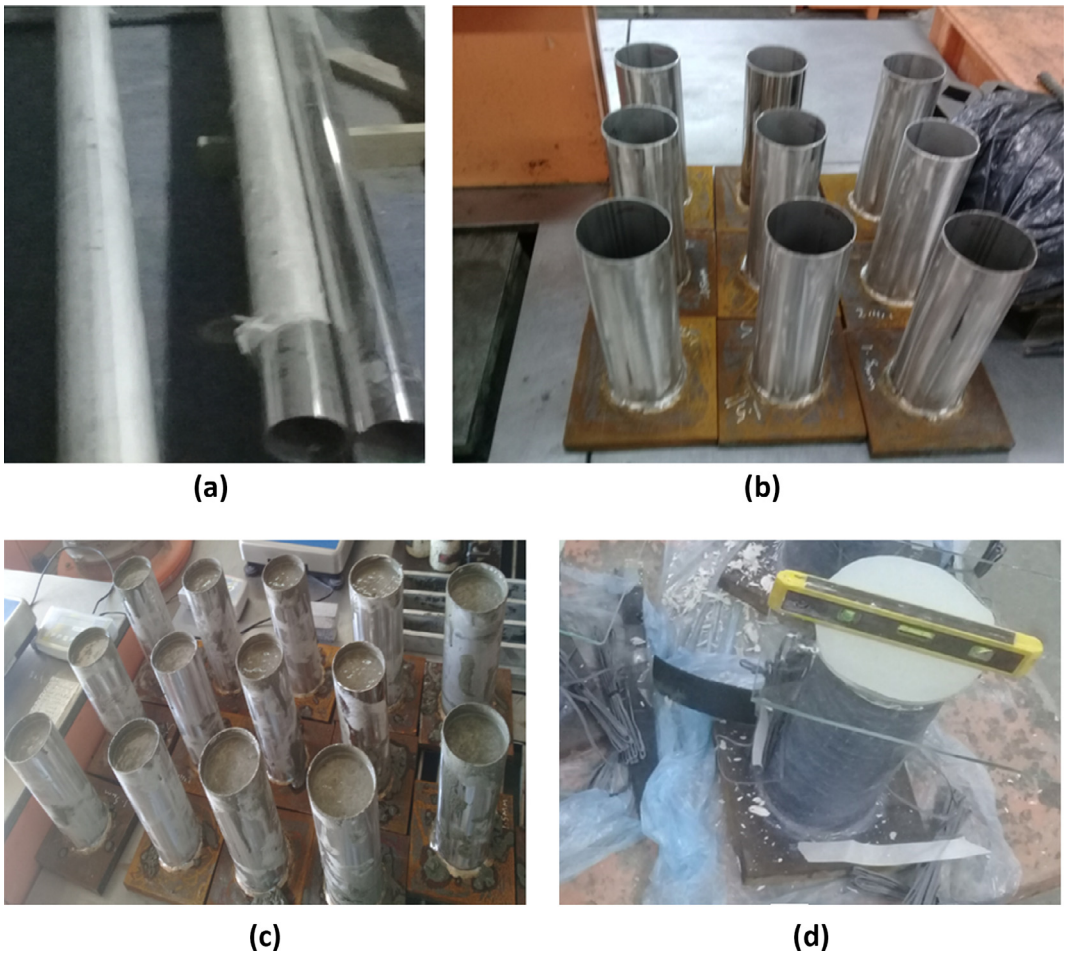

Fig. 4. Stub columns preparation (a) long cold-rolled stainless steel tubes, (b) stub columns with the bottom welded plate, (c) stub columns concrete casting and (d) applying a thin gypsum capping.

3000 MPa. The adhesive tensile strength and the tensile modulus of elasticity are 30 MPa and 4500 MPa, respectively.

2.3. Stub column specimens

2.3.1. Specimens preparation

Thirteen stainless steel circular tubes with the dimensions given in Table 1 were cut from three long cold-rolled tubes as shown in Fig. 4a. Subsequently, one thick steel plate was welded to the bottom end of the tubes as shown in Fig. 4b, while the top end was left without a plate to cast the concrete in. The tubes were filled with normal concrete with appropriate shaking to avoid any concrete segregation, as displayed in Fig. 4c. After curing, the outer surface of the stainless steel tubes was cleaned to remove any fragments stuck during the concrete casting. To increase adhesion with CFRP, the outer surface of the stainless steel tubes was roughened by sandpapers. A continuous carbon fiber sheet 300 mm in width was wrapped with a sufficient amount of glue around the stainless steel tubes with the required number of layers. An appropriate overlapping length was added to satisfy circumferential continuity. To ensure uniform compressive loading on the specimens, a thin gypsum layer was applied to the top surface to fill any voids, as illustrated in Fig. 4d. A minimum amount of gypsum was used to reduce its effect on the early stages of loading.

2.3.2. Instrumentation and testing

For each specimen, an axial compressive test with monotonic loading was performed to determine the load-deformation response. The top end of the samples was clamped with an appropriate steel belt, while the bottom end was welded with a thick steel plate. This clamping for both ends is required to avoid any possibility of failure at the end surfaces due to out of flatness. The steel clamp at the top end was placed slightly away from the top end to prevent any load transferred from the steel clamp to the stainless steel tube. Fig. 5 shows the test setup, comprised of four linear variable displacement transducers (LVDTs) which were located vertically to measure the average end shortening. Two strain gauges were glued longitudinally to all the specimens at

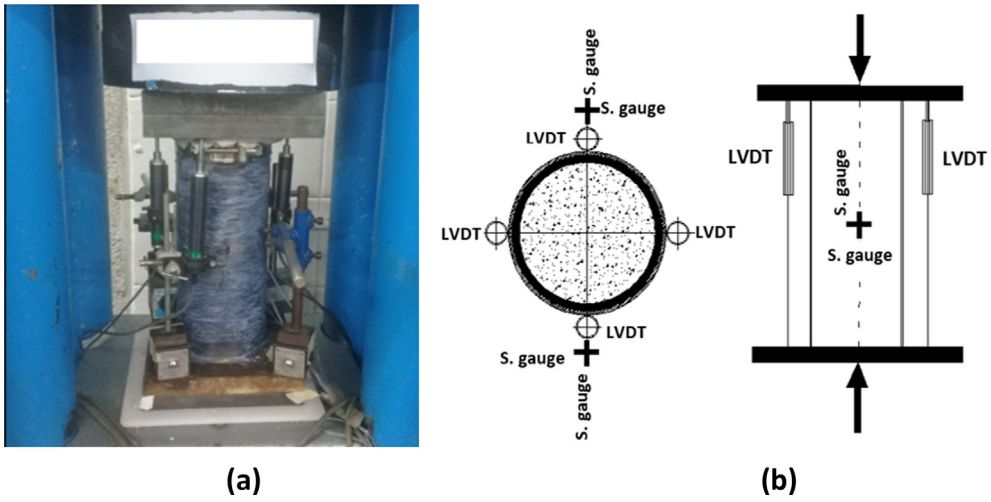

Fig. 5. Axially loaded stub column test arrangement: (a) test setup, (b) schematic Diagram of Experimental Setup.

mid-height while two stain gauges were pasted horizontally at mid-height. For the wrapped specimens, stain gauges were affixed to the outer surface of the CFRP composite. A MATEST 3000 kN hydraulic testing machine was used to apply an axial compressive load with a loading rate of 1 kN/s. The LVDTs, strain gauges and load cell readings were connected to the data logger.

2.3.3. Results and discussion

2.3.3.1. Force-deformation responses. The axial load-end shortening curves for all of the stub column specimens are displayed in Figs. 6–8, where the end shortening was taken as the average value of the four LVDTs. Vertical strain gauge readings were employed to correct the force-end shortening curves in the initial loading stage to obtain true end shortening values. At the initial loading stage, the effect of end platen deformation and the gypsum layer deformation lead to a shift in the end shortening values. The vertical mid-height stain gauge readings were multiplied by the specimen length to obtain the average end shortening. The force-end shortening curves shown in Figs. 6–8 represent the true force-end shortening after the correction.

The full force-end shortening curves of the wrapped specimens can be divided into three stages. In the first stage, the stainless steel and concrete core behave elastically with no composite action between them since the lateral expansion of the stainless steel tube is greater than the lateral expansion of the concrete core due to the larger Poisson's ratio of the stainless steel material. In this stage, as shown in Figs. 6–8, the force-end shortening relationships of the unwrapped and the wrapped specimen are matching because of the absence of the CFRP role at this stage. In the second stage, with the increase in the loading, the concrete core starts to behave inelastically and the concrete lateral expansion becomes greater than that of the stainless steel tube. The concrete core becomes confined by the stainless steel tube and the CFRP wrap. As clarified in Figs. 6–8, the strength of the wrapped specimens becomes greater than that of the unwrapped specimens. In this stage, the increase in the strength of the wrapped specimens is driven by the CFRP confinement and this is clear where the force-end shortening relationships become straight lines, as shown in Figs. 6–8. In the third stage, when the CFRP wrap reaches its ultimate strength, CFRP rupture suddenly occurs leading to a sudden drop in the load carrying capacity, as shown in Figs. 6–8. After that, the wrapped specimens behave like the unwrapped specimens and their force-end shortening relationships come into agreement again.

By comparing the results of the CFRP-wrapped CFSST columns with the unwrapped ones, it is clear that the CFRP wraps provide a significant improvement in terms of load carrying capacity, as well as in

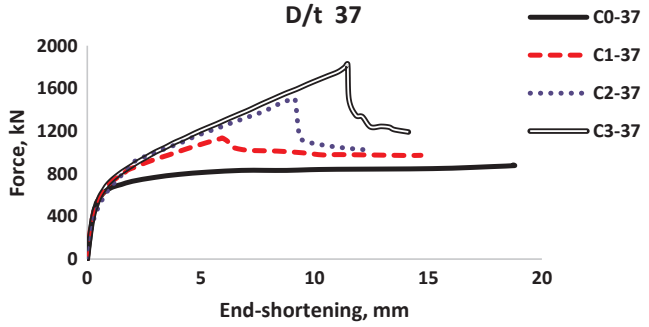

Fig. 6. Experimental force-end shortening of series G1 specimens.

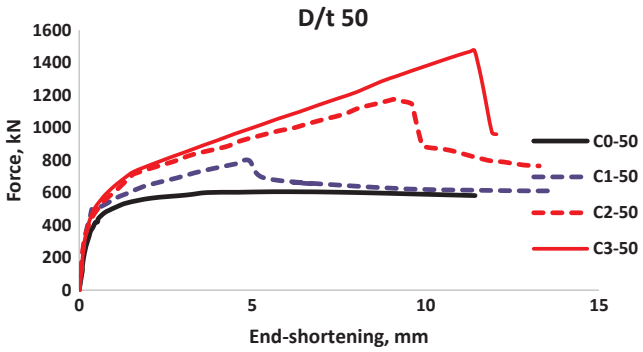

Fig. 7. Experimental force-end shortening of series G2 specimens.

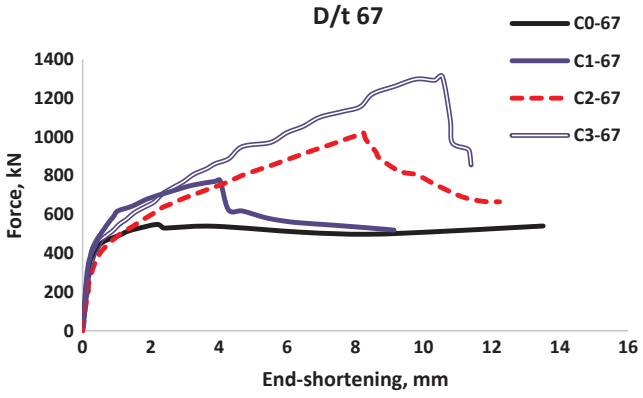

Fig. 8. Experimental force-end shortening of series G3 specimens.

Table 4
Test results of load carrying capacity and ultimate end shortening.

Series	Specimen label	Confinement ratio	$P_{test,}$ (kN)	$\delta_{test,}$ (mm)
	C0-37	0	831	3.7
G1	C1-37	0.43	1133	6.3
	C2-37	0.85	1502	9.1
	C3-37	1.28	1825	11.5
	C0-50	0	600	3.6
G2	C1-50	0.38	799	4.9
	C2-50	0.76	1176	9.1
	C3-50	1.13	1474	11.4
	C0-67	0	562	3.7
	C1-67	0.38	775	5.6
G3	C2-67	0.76	1020	8.2
	C3-67	1.13	1311	10.6
G4	C2-50-Partial	0.76	662	5.9

the axial shortening capacity as shown in Figs. 6–8. The load carrying capacity and axial shortening capacity of the stub specimens are summarized in Table 4 as P_{test} and δ_{test}, respectively.

The axial load-end shortening curves of the partially wrapped, fully wrapped and unwrapped specimens for the same D_s/t_s ratio are displayed in Fig. 9. For the same CFRP thickness and layers, the carrying load capacity of the fully wrapped specimen is much greater than the load carrying capacity of the partially wrapped specimens, as shown clearly in Fig. 9. Although two-thirds of the specimen length were covered by CFRP, the strength enhancement compared with the unwrapped specimen was 10%, while the fully wrapped specimen enhanced the strength by 96%. Therefore, it is not recommended to use partial wrapping for CFSST columns.

2.3.3.2. Failure modes. The function of the stainless steel, concrete infill and CFRP wrap in the CFRP-confined CFSSTs can be explained as follows. The stainless steel tube has two main functions: contributing, based on its axial stiffness, to carrying the axial load and confining the concrete. For the concrete core, it carries a major part of the axial compressive load, as well as preventing inward local buckling of the stainless steel tube. The CFRP wrap postpones the occurrence of outward local buckling of the stainless steel tube and increases the concrete confinement.

All of the unwrapped specimens experienced continuous dilation and localized outward buckling of the stainless steel tube close to one end, as shown in Fig. 10. Because of the initial imperfections, the inelastic local buckling cannot occur simultaneously near to both ends, but only at one end. When the outward local buckling of the stainless steel tubes occurs, the load carrying capacity drops slightly and then rises again. This re-increasing of the strength takes place because of the redistribution of the load carrying where the stainless steel tubes stop carrying the load and the entire loading takes place on the confined concrete core. The ultimate state of the non-confined specimens is

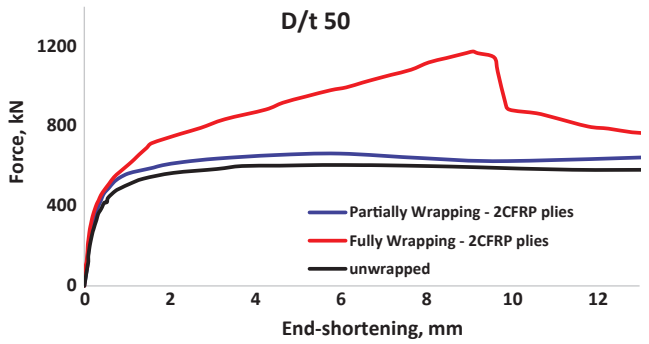

Fig. 9. Comparison of fully and partially wrapped specimens with D_s/t_s of 50.

defined as the state when the outward local buckling of the stainless steel tube occurs associated with excess inelastic deformation; regardless of the load increasing that takes place after inelastic local buckling.

All CFRP-confined specimens failed because of the sudden rupture of the CFRP wrap due to the lateral concrete core expansion at the mid-height as displayed in Fig. 10. This concrete lateral expansion makes the carbon CFRP expand until it reaches its ultimate strain. This sudden rupture of the CFRP leads to a rapid drop in load carrying capacity. The ultimate state of the CFRP-confined specimens is defined as the state when the rupture of the CFRP jacket occurs followed by a sudden load drop.

The mode of failure of the partially wrapped specimen was the outward local buckling of the stainless steel just after CFRP confinement in the middle-third, as shown in Fig. 11.

2.3.3.3. Effect of CFRP strengthening on the load carrying capacity. By adding the CFRP wrap, the load carrying capacity of the CFSST specimens was increased significantly compared with the control specimens. For the CFSSTs made of stainless steel tubes with a D/t_s ratio of 37, the load carrying capacity enhancement by adding one CFRP ply, two CFRP plies and three CFRP plies was 36%, 81% and 120%, respectively. Regarding the specimens with a D/t_s of 50, the enhancement was 33%, 96% and 145% due to using one CFRP ply, two CFRP plies and three CFRP plies, respectively. For specimens with a D/t_s of 67, the improvement was 38%, 81% and 133% compared with the control specimen, by using a CFRP wrap with one ply, two pies and three plies, respectively.

A confinement ratio can also be used to represent the effect of the CFRP thickness. It can be defined as the ratio between confinement pressure (f_l) at the CFRP rupture to the unconfined concrete compressive strength (f'_c). The confinement ratios for the tested specimens are summarized in Table 4. It is clear that the confinement ratio is directly proportional to the amount of strength enhancement.

$$f_l = \frac{2t_f f_{frp}}{D_s} \tag{1}$$

where f_{frp} is the tensile strength of CFRP jacket at CFRP rupture.

2.3.3.4. Effect of CFRP strengthening on the axial shortening capacity. The CFRP-wrapped CFSST columns exhibited a significant enhancement in the axial shortening capacity. For the wrapped specimens with a D/t_s ratio of 37, the axial shortening capacity enhancement by adding one, two and three CFRP plies with respect to the unwrapped specimen was, respectively, 70%, 145% and 210%. For the wrapped specimens with a D/t_s ratio of 50, the axial shortening capacity enhancement was 36%, 150% and 216% due to the addition of one, two and three CFRP plies with respect to the unwrapped specimen, respectively. For the specimens with a D/t_s of 67, the axial shortening capacity improvement was 50%, 120% and 180% compared with the unwrapped one, by using a CFRP jacket with one, two and three plies with respect to the unwrapped specimen, respectively.

3. Finite element modeling

Finite element modeling (FEM) was performed in parallel with the experimental work. The aim of the FEM is to validate the models and thereafter perform a parametric study. This parametric study reduces the cost and saves time compared with conducting a large number of experiments. The parametric study results were exploited to propose an analytical model based on the curve fitting parameters as described later. The nonlinear finite element models were carried out using the ABAQUS software [45].

Fig. 10. Failure mode of: (a) series G1 specimens, (b) series G2 specimens and (c) series G3 specimens.

3.1. Finite element types

The axially loaded composite columns were modeled using shell and solid elements obtainable in the element library of the ABAQUS software [45] as shown in Fig. 12. The concrete core was represented using 3D C3D8 solid elements. The circular stainless steel tube was modeled using S4R shell elements that have six degrees of freedom (DOF) at each node making them able to provide accurate predictions for buckling modes. Furthermore, S4R shell elements were employed to model the CFRP wrap. A rigid shell plate was modeled and placed at both ends of the tubular columns to transfer the axial load uniformly.

The results of mesh size sensitivity are presented in Fig. 13 where each point refers to the mesh size. It indicates that an approximate mesh size of 7 mm provides accurate predictions with a reasonable running time.

3.2. Boundary conditions and load application

Each end of the rigid plate was coupled to a reference point so that all end degrees of freedom (DOFs) were applied to the reference points as point DOFs. At the upper rigid plate, all DOFs were restrained, except for translation in the longitudinal direction. On the other hand, all DOFs at the lower rigid plate were restrained (fully fixed end). The compressive loading was applied as a displacement control to capture the strain softening behavior.

Fig. 11. Failure mode of the partially wrapped specimen.

3.3. Initial imperfections

Initial geometric imperfections are out-of-plane deflections introduced into thin-walled structural elements during the manufacturing process [47]. The structural performance of thin-walled members can be strongly influenced by the initial geometric imperfections, depending on how thin the element is. Therefore, it is necessary to include these initial geometric imperfections with appropriate patterns and amplitudes into the FE models to obtain an acceptable match with the measured experimental results. The initial geometric imperfection pattern along the member length was taken as the elastic local buckling mode that provides a symmetric half-sine wave shape under axial compressive loading. This was carried out by performing an elastic buckling analysis and linking the required elastic buckling mode shape deformation results with the actual nonlinear FE model using a short subroutine available in the ABAQUS software [45] called IMPERFECTION. The amplitude to be multiplied by the imperfection pattern was taken as a percentage of the stainless steel tube thickness. In this study, the amplitude was taken as (t/10, t/50 and t/100) for each model to evaluate the effect of the initial geometric imperfections.

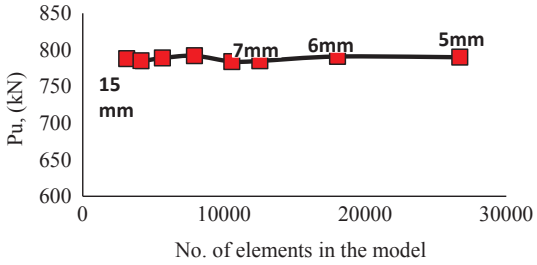

Fig. 13. Effect of mesh size on the load carrying capacity of CFRP-wrapped CFSST columns.

3.4. Material modeling

3.4.1. Stainless steel material

An elastic-plastic model with the Von Mises yield criterion was employed to define the constitutive behavior of the stainless steel material as presented in references [46–48]. The engineering stress-strain relationship (σ_{Eng}, ε_{Eng}) of stainless steel material obtained from tensile testing was converted to a true stress-true strain (σ_{true}, ε_{true}) format using Eqs. (2) and (3).

$$\sigma_{true} = \sigma_{Eng}(1 + \varepsilon_{Eng}) \tag{2}$$

$$\varepsilon_{true} = ln(1 + \varepsilon_{Eng}) \tag{3}$$

3.4.2. Concrete material

In concrete-filled stainless steel tubes, the concrete infill has to be modeled as confined concrete, while mechanical properties testing is conducted on uniaxial unconfined concrete. Therefore, an equivalent confined stress-strain curve has to be used. The confined stress-strain curve was modeled using the approach reported in reference [49]. The stress-strain curves for confined and unconfined concrete are shown in Fig. 14 where f_c', f_{cc}, ε_c and ε_{cc} are, respectively, the unconfined concrete compressive strength, confined concrete compressive strength, unconfined compressive strain corresponding to f_c' and the confined compressive strain corresponding to f_{cc}. The values of f_{cc} and ε_{cc} were calculated using expressions proposed by Mander et al. [50]. The confined concrete strain-stress curve consists of three parts that need to be identified, as illustrated in Fig. 14. The first part is a linear elastic part that extends to the elastic limit stress. This elastic limit stress was taken as 0.5 of f_{cc} as reported in [49]. The initial modulus of elasticity of the confined concrete, E_{cc}, was calculated according to ACI [51]:

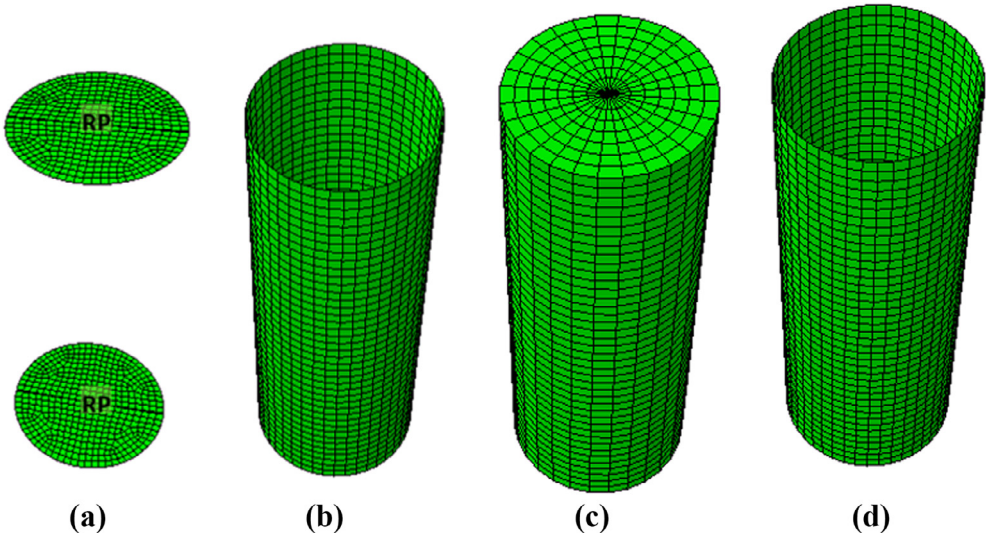

Fig. 12. Finite Element modeling (a) rigid plates with reference points, (b) stainless steel tube elements, (c) concrete core elements and (d) CFRP elements.

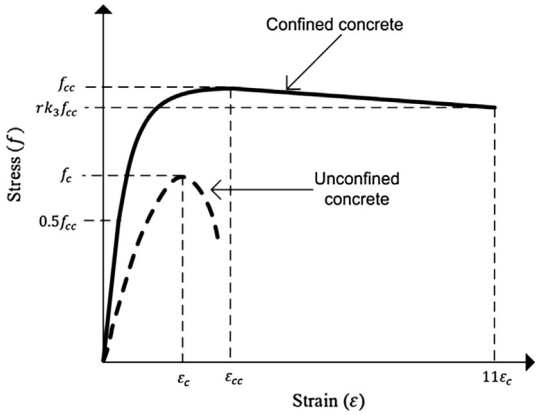

Fig. 14. Confined and unconfined stress-strain curves of concrete material [54].

$$E_{cc} = 4700\sqrt{f_{cc}} \quad \text{MPa} \tag{4}$$

The second part of the confined stress-strain curve is a non-linear part extending from the end of the first part ($0.5f_{cc}$) which continues onto the ultimate confined compressive strength (f_{cc}) and this nonlinear part was determined as proposed by Saenz [52]. The third part representing the strain softening is a linear part that extends to a value ($rk_3\, f_{cc}$) which is lower than the ultimate confine strength as shown in Fig. 14. The factors r and k_3 were determined from empirical equations given in Refs. [53,49], respectively.

A constitutive description of the concrete material in the elastic linear region, before $0.5\, f_{cc}$ as shown in Fig. 14, needs only two elastic parameters to describe it: the initial modulus of elasticity (E_{cc}) and the Poisson's ratio which was taken as 0.2. On the other side, the constitutive description behavior of the concrete material in the plastic region includes the description of the yield surface function, flow rule and hardening/softening laws. The plasticity of the concrete material was modeled in the ABAQUS software [45] using the Concrete Damaged Plasticity Model (CDPM) [54]. CDPM is used to model the plasticity and damage behaviors of the concrete material. In CDPM, the damage definition is used to characterize the stiffness degradation for the unloading response. The damage effect in this study can be neglected because the loading is monotonic. Some parameters other than the confined stress-strain relationships are required to describe the concrete plasticity using CDPM. To define the yield surface function, two parameters are introduced: the strength ratio of concrete under equal biaxial compression to triaxial compression (K_c) and the ratio of concrete strength under equal biaxial compression to the uniaxial strength (f_b'/f_{co}'). In this study to achieve a good match with the experimental results, values of 0.8 and 1.16 were used to define K_c and f_{bo}/f_c', respectively. In addition, two parameters are needed to describe the non-associated flow rule: the dilation angle and the eccentricity parameter, and they were introduced into the ABAQUS software [45] with the following values of 15^0 and 0.10, respectively.

3.4.3. CFRP material

CFRP wraps were modeled in the ABAQUS software environment [45] as a linear elastic composite laminate. The failure mode observed in the experimental work of the CFRP wraps was the tensile rupture. Hence, it was essential to model the damage behavior of CFRP in the FE modeling. To model the CFRP wrap properly, it is necessary to define the laminate elastic, strength and damage evolution properties. The laminate elastic properties in the fibers' direction were taken from the manufacturer as mentioned earlier, but in the other direction they were taken as a percentage of the properties in the fibers' direction. The Hashin Damage Model [55], which is available in the ABAQUS software [45], was used to model the strength and damage properties. The tensile strength value in the fibers' direction was given from the manufacturer, while the other values of strength in the orthogonal direction were assumed to be small values as reported in [56] to make the FE results match closely with the tests results. The values of damage evolution shown in Table 5 were adopted as given in Ref. [57].

3.5. FE interaction modeling

The interaction modeling between the stainless tube and concrete infill was specified as a friction interaction in the tangential direction with a friction coefficient of 0.25 as reported in [53], while the interaction in the normal direction was assigned as a hard contact to prevent any penetration between the two surfaces. The concrete core and stainless steel tube were assigned as master and slave surfaces, respectively. The contact between the stainless steel tube and the CFRP jacket was represented using a tie interaction where the stainless steel surface was assigned to be the master surface. The interaction between the rigid plate surfaces and the steel tube surfaces was specified as a tie contact where the rigid plates were assigned to be the master surfaces. On the other hand, the interaction between the rigid plates and the concrete infill surfaces was introduced using a friction interaction in the tangential direction with a friction coefficient of 0.35 as recommended in [58] and hard contact in the normal direction.

3.6. Validation of the FE models

An evaluation of the accuracy of the FE models was performed by comparing the results obtained from the experimental work and the FE models in terms of the load carrying capacity, force-displacement curves and the mode of failure. The ratios of the FE to the test load carrying capacity for the three imperfection levels are reported in Table 6. It is clear that the predicted FE failure loads and deformations for the three considered imperfection amplitudes (t/10, t/50 and t/100) were not sensitive to the change in imperfection amplitudes. Thus, an

Table 5
CFRP modeling parameters.

Parameters	Unit	Values introduced in ABAQUS
Laminate elastic properties		
Poisson's ratio		0.3
E1 (fiber direction), E2	MPa	220,000, 10,000
G12, G13	MPa	5000, 5000
Hashin damage model		
Strength		
Tensile strength (fiber direction), Tensile strength (transverse direction)	MPa	3000, 10
Compressive strength (fiber direction), compressive strength (transverse direction)	MPa	10, 10
Shear (fiber direction), Shear (transverse direction)	MPa	10, 10
Damage Evolution		
Tensile fracture energy (fiber direction), Tensile fracture energy (transverse direction)	mJ/mm^2	92, 1.1
Compressive fracture energy (fiber direction), compressive fracture energy (transverse direction)	mJ/mm^2	1.1, 0.2

Table 6
Comparison of the test and FE load carrying capacity and ultimate deformation.

Specimen	P_{FE}/P_{test}			$\delta_{FE}/\delta_{test}$		
	Imperfection Amplitudes			Imperfection Amplitudes		
	t/10	t/50	t/100	t/10	t/50	t/100
C0-37	1.02	1.02	1.02	0.99	0.99	0.99
C1-37	1.05	1.06	1.06	0.98	0.91	0.91
C2-37	1.02	1.03	1.03	1.05	1.01	1.01
C3-37	1.04	1.04	1.04	0.98	0.94	0.94
C0-50	1.04	1.05	1.05	1.04	1.04	1.04
C1-50	1.13	1.14	1.14	1.15	1.12	1.12
C2-50	1.02	1.02	1.02	1.04	1.02	1.01
C3-50	1.02	0.99	1.01	0.96	0.95	0.94
C0-67	0.93	0.93	0.93	0.98	0.98	0.98
C1-67	1.03	1.03	1.03	1.01	1.01	1.01
C2-67	1.04	1.04	1.04	1.12	1.09	1.09
C3-67	1.03	1.02	1.02	1.00	0.99	0.99
Mean	1.03	1.03	1.03	1.03	1.00	1.00
COV	0.04	0.05	0.05	0.06	0.06	0.06

imperfection amplitude of t/100 was adopted for validation with the experimental results. The FE model results showed a good agreement with the experimental results up to the ultimate load, thereafter, the FE model showed some variation from the experimental results. This may attribute to the used values of CFRP damage evolution modeling. A good agreement between the FE force-displacement curves and those obtained from the experimental work was observed as illustrated in Fig. 15. For the comparison between the test and FE studies in terms of failure modes, a good agreement was observed, as shown in Fig. 16. In general, it can be concluded that the FE models carried out using the ABAQUS software [45] are able to predict the load carrying capacity of CFRP-confined CFSST columns accurately, to capture the modes of failure observed in testing and to provide force-deformation curves that match well with the test curves.

3.7. Comparison of stainless steel and carbon steel columns

A comparison is made between CFRP-wrapped CFSST and CFCST columns. Identical columns, one using stainless steel and the other carbon steel tubes, were structurally evaluated. The stress-strain diagrams for both stainless and carbon steel are shown in Fig. 17. The load versus end shortening for both columns are shown in Fig. 18. The two columns showed identical behavior within the elastic range similar to

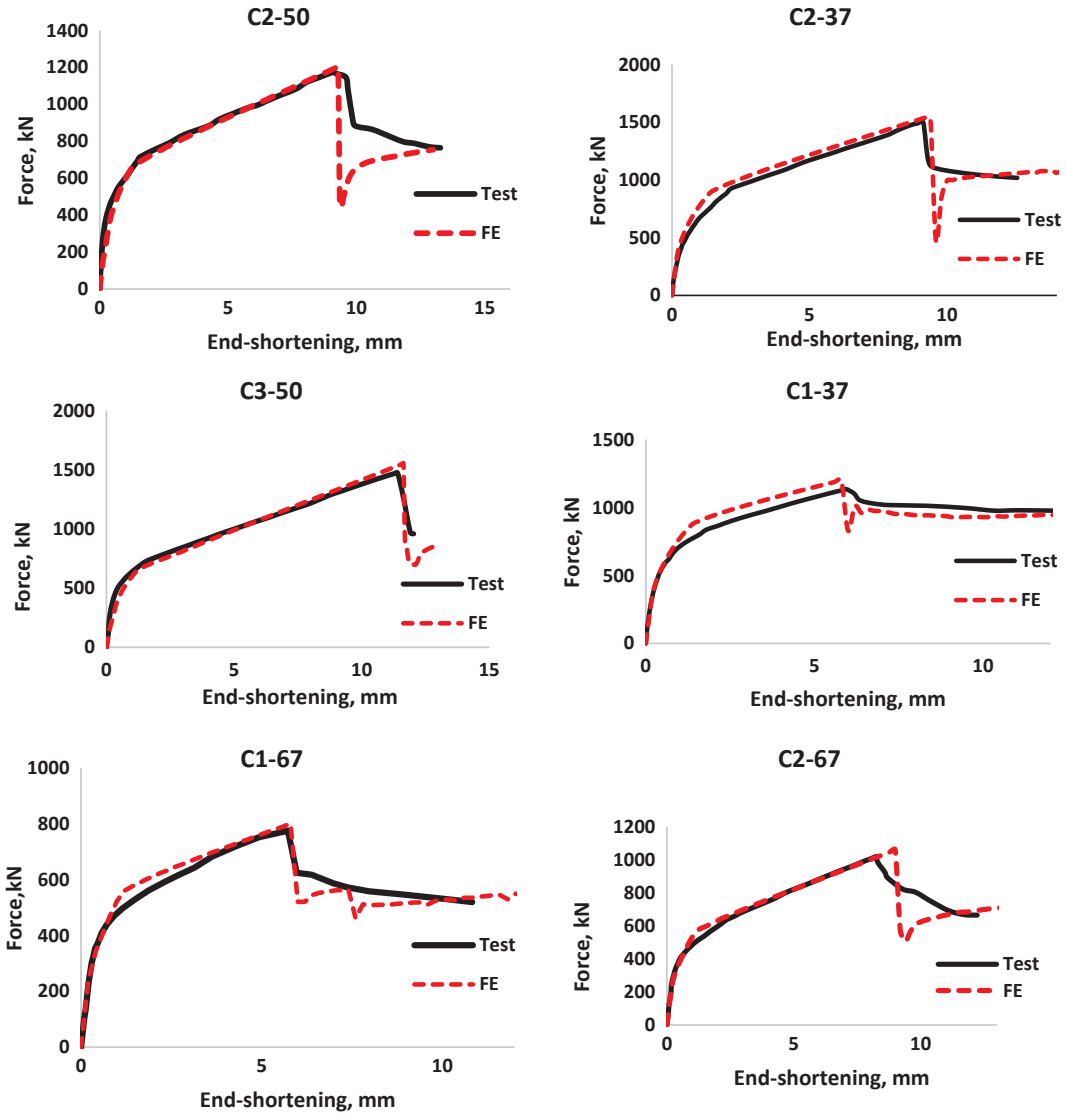

Fig. 15. Experimental and numerical force-end shortening for some selected specimens.

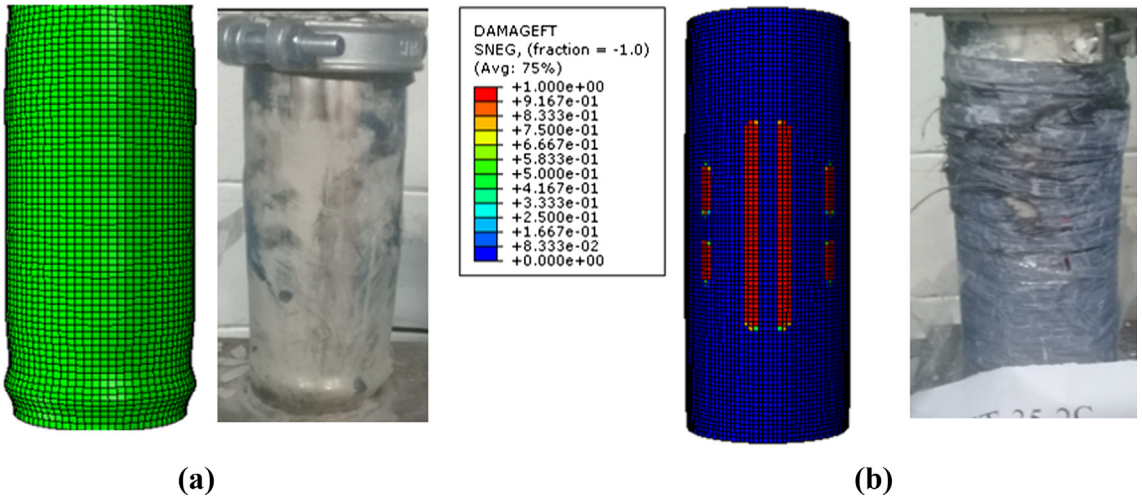

Fig. 16. General failure mode of (a) unwrapped specimens and (b) wrapped specimens.

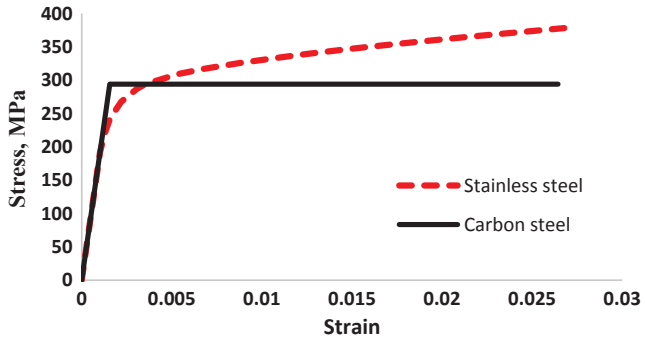

Fig. 17. Stainless steel and carbon steel stress-strain relationships.

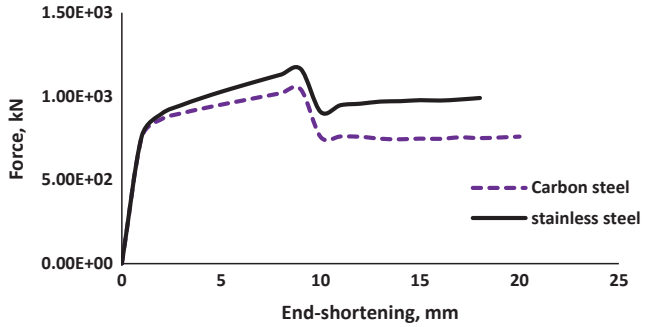

Fig. 18. Comparison of force-displacement relationships of stainless steel and carbon steel.

their stress-strain diagrams. However, stainless steel showed better performance in the inelastic range, as expected from the mechanical properties.

3.8. FE parametric study

Using the validated FE models, 108 models were analyzed using FE to obtain the load carrying capacity (P_{FE}) of CFRP-wrapped CFSST columns. P_{FE} data was employed to develop a proposed model to predict the load carrying capacity. The austenitic stainless steel material properties of CHSST 101 × 1.5 and CHSST 114 × 3.05 shown in Table 3 were adopted in the FE parametric study. The normal concrete compressive strength was extended in this FE parametric study to be three levels: 25 MPa, 43.6 MPa and 60 MPa, as well as the D/t_s ratio of the stainless steel tubes which was taken as six levels: 37.5, 50.5, 67.3, 100, 150 and 200. The number of CFRP plies (n) were grouped in four levels of one, two, three and six plies, where the thickness of one ply is 0.29 mm. The ultimate strength of unidirectional CFRP in the fiber direction (f_{frp}) was 3000 MPa and 1500 MPa. To avoid any flexural global buckling, the L/D ratio of the stainless steel tubes was taken as 3. The parametric study variables discussed above, as well as the P_{FE}, are summarized in Table 7.

4. Analytical study

A mathematical model to predict the load carrying capacity of CFRP-wrapped CFSST columns under axial compression is not available in the literature. Therefore, in this study, an analytical model based on curve fitting parameters to predict the load carrying capacity of CFRP-wrapped CFSST columns was proposed. The stress-strain characteristics of the stainless steel material are different from those of carbon steel material, as discussed in the introduction.

4.1. Proposed model

The load carrying capacity results obtained from the parametric study, as shown in Table 7, were employed to develop a simple model to predict the load carrying capacity analytically (P_u) of CFRP-confined CFSST columns under axial compressive load. From an equilibrium state, the load carrying capacity (P_u) is defined as:

$$P_u = P_s + P_{core} \tag{5}$$

where P_s refers to the axial ultimate strength of the stainless steel tube and P_{core} represents the axial ultimate strength of the concrete fill. P_s was formulated using the continuous strength method (CSM) approach [11–16] as shown in Eq. (6). The CSM approach has been developed as a deformation-based design method to exploit the noticeable strain hardening in the determination of stainless steel cross-section resistances, as discussed earlier in the introduction.

$$P_s = A_s \sigma_{LB} \tag{6}$$

where A_s is the cross sectional area of the stainless steel tube and σ_{LB} is the local buckling stress. The CSM approach replaces the cross-sectional classification with a continuous relationship between the deformation capacity and the cross-section slenderness, as shown in Eq. (7a) [12]:

$$\frac{\varepsilon_{LB}}{\varepsilon_{0.2}} = \frac{4.44 \times 10^{-3}}{\lambda_c^{4.5}} \leq min(15, \frac{0.1\varepsilon_u}{\varepsilon_{0.2}}) \tag{7a}$$

where λ_c, ε_{LB}, $\varepsilon_{0.2}$, and ε_u are defined as the cross-section slenderness, local buckling strain, equivalent 2% proof strain (equivalent yield

Table 7
Comparison of the FE parametric study results and the proposed model results.

Specimen	D (mm)	t_s (mm)	D/t_s	f_c' (MPa)	Stainless steel		CFRP		P_{FE} (kN)	
					$\sigma_{0.2}$ (MPa)	$\sigma_{1.0}$ (MPa)	f_{frp} (MPa)	n		P_{FE}/P_u
S1	114.3	3.05	37.5	25	322	365	3000	1	1142	1.08
S2	114.3	3.05	37.5	25	322	365	3000	2	1507	1.01
S3	114.3	3.05	37.5	25	322	365	3000	3	1862	1.00
S4	114.3	3.05	37.5	25	322	365	3000	6	2938	0.88
S5	114.3	3.05	37.5	43.6	322	365	3000	1	1241	1.06
S6	114.3	3.05	37.5	43.6	322	365	3000	2	1585	1.04
S7	114.3	3.05	37.5	43.6	322	365	3000	3	1944	1.03
S8	114.3	3.05	37.5	43.6	322	365	3000	6	2981	0.98
S9	114.3	3.05	37.5	60	322	365	3000	1	1274	0.98
S10	114.3	3.05	37.5	60	322	365	3000	2	1630	1.01
S11	114.3	3.05	37.5	60	322	365	3000	3	1985	1.01
S12	114.3	3.05	37.5	60	322	365	3000	6	3044	1.01
S13	101	2	50.1	25	322	365	3000	1	792	1.08
S14	101	2	50.1	25	322	365	3000	2	1101	1.01
S15	101	2	50.1	25	322	365	3000	3	1450	1.00
S16	101	2	50.1	25	322	365	3000	6	2290	0.88
S17	101	2	50.1	43.6	322	365	3000	1	865	1.06
S18	101	2	50.1	43.6	322	365	3000	2	1162	1.04
S19	101	2	50.1	43.6	322	365	3000	3	1465	1.03
S20	101	2	50.1	43.6	322	365	3000	6	2349	0.98
S21	101	2	50.1	60	322	365	3000	1	898	0.98
S22	101	2	50.1	60	322	365	3000	2	1198	1.01
S23	101	2	50.1	60	322	365	3000	3	1487	1.01
S24	101	2	50.1	60	322	365	3000	6	2380	1.01
S25	101	1.5	67.3	25	322	365	3000	1	698	1.08
S26	101	1.5	67.3	25	322	365	3000	2	979	1.01
S27	101	1.5	67.3	25	322	365	3000	3	1256	0.96
S28	101	1.5	67.3	25	322	365	3000	6	2077	0.88
S29	101	1.5	67.3	43.6	322	365	3000	1	813	1.10
S30	101	1.5	67.3	43.6	322	365	3000	2	1061	1.05
S31	101	1.5	67.3	43.6	322	365	3000	3	1341	1.03
S32	101	1.5	67.3	43.6	322	365	3000	6	2189	1.00
S33	101	1.5	67.3	60	322	365	3000	1	876	1.04
S34	101	1.5	67.3	60	322	365	3000	2	1162	1.07
S35	101	1.5	67.3	60	322	365	3000	3	1434	1.06
S36	101	1.5	67.3	60	322	365	3000	6	2235	1.03
S37	200	2	100	25	322	365	3000	1	1797	1.07
S38	200	2	100	25	322	365	3000	2	2394	1.08
S39	200	2	100	25	322	365	3000	3	3011	1.09
S40	200	2	100	25	322	365	3000	6	4756	1.05
S41	200	2	100	43.6	322	365	3000	1	2024	0.95
S42	200	2	100	43.6	322	365	3000	2	2620	1.01
S43	200	2	100	43.6	322	365	3000	3	3207	1.04
S44	200	2	100	43.6	322	365	3000	6	4966	1.09
S45	200	2	100	60	322	365	3000	1	2379	0.91
S46	200	2	100	60	322	365	3000	2	2832	0.94
S47	200	2	100	60	322	365	3000	3	3400	0.98
S48	200	2	150	60	322	365	3000	6	5152	1.07
S49	150	1	150	25	322	365	3000	1	977	1.06
S50	150	1	150	25	322	365	3000	2	1420	1.11
S51	150	1	150	25	322	365	3000	3	1862	1.12
S52	150	1	150	25	322	365	3000	6	3208	1.13
S53	150	1	150	43.6	322	365	3000	1	1111	0.94
S54	150	1	150	43.6	322	365	3000	2	1539	1.04
S55	150	1	150	43.6	322	365	3000	3	1978	1.10
S56	150	1	150	43.6	322	365	3000	6	3312	1.18
S57	150	1	150	60	322	365	3000	1	1309	0.91
S58	150	1	150	60	322	365	3000	2	1711	0.99
S59	150	1	150	60	322	365	3000	3	2134	1.06
S60	150	1	150	60	322	365	3000	6	3431	1.17
S61	600	3	200	25	322	365	3000	1	9576	0.97
S62	600	3	200	25	322	365	3000	2	10,921	0.98
S63	600	3	200	25	322	365	3000	3	12,658	1.03
S64	600	3	200	25	322	365	3000	6	17,855	1.10
S65	600	3	200	43.6	322	365	3000	1	14,226	0.97
S66	600	3	200	43.6	322	365	3000	2	14,413	0.92
S67	600	3	200	43.6	322	365	3000	3	14,871	0.89
S68	600	3	200	43.6	322	365	3000	6	19,922	0.99
S69	600	3	200	60	322	365	3000	1	18,706	0.97
S70	600	3	200	60	322	365	3000	2	18,721	0.92
S71	600	3	200	60	322	365	3000	3	19,030	0.90
S72	600	3	200	60	322	365	3000	6	22,020	0.910

(*continued on next page*)

Table 7 (*continued*)

Specimen	D (mm)	t_s (mm)	D/t_s	f_c' (MPa)	Stainless steel		CFRP		P_{FE} (kN)	
					$\sigma_{0.2}$ (MPa)	$\sigma_{1.0}$ (MPa)	f_{frp} (MPa)	n		P_{FE}/P_u
S73	114.3	3.05	37.8	25	293	332	3000	6	2893	0.90
S74	114.3	3.05	37.5	43.6	293	332	3000	6	2939	0.98
S75	114.3	3.05	37.5	60	293	332	3000	6	3000	1.02
S76	101	2	50.5	25	293	332	3000	6	0	1.06
S77	101	2	50.5	43.6	293	332	3000	6	2322	0.99
S78	101	2	50.5	60	293	332	3000	6	2351	1.02
S79	101	1.5	50.5	25	293	332	3000	6	2056	0.89
S80	101	1.5	50.5	43.6	293	332	3000	6	2164	1.01
S81	101	1.5	50.5	60	293	332	3000	6	2212	1.05
S82	200	2	100	25	293	332	3000	6	4701	1.06
S83	200	2	100	43.6	293	332	3000	6	4917	1.10
S84	200	2	100	60	293	332	3000	6	5094	1.08
S85	150	1	150	25	293	332	3000	6	3183	1.14
S86	150	1	150	43.6	293	332	3000	6	3287	1.19
S87	150	1	150	60	293	332	3000	6	3433	1.19
S88	600	3	200	25	293	332	3000	6	17,619	1.10
S89	600	3	200	43.6	293	332	3000	6	19,702	0.99
S90	600	3	200	60	293	332	3000	6	21,783	0.91
S91	114.3	3.05	37.8	25	293	332	1500	6	1763	0.91
S92	114.3	3.05	37.5	43.6	293	332	1500	6	2939	0.98
S93	114.3	3.05	37.5	60	293	332	1500	6	2026	1.04
S94	101	2	50.5	25	293	332	1500	6	0	1.07
S95	101	2	50.5	43.6	293	332	1500	6	1469	1.01
S96	101	2	50.5	60	293	332	1500	6	1551	1.04
S97	101	1.5	50.5	25	293	332	1500	6	1266	0.95
S98	101	1.5	50.5	43.6	293	332	1500	6	1372	1.04
S99	101	1.5	50.5	60	293	332	1500	6	1483	1.08
S100	200	2	100	25	293	332	1500	6	2996	1.07
S101	200	2	100	43.6	293	332	1500	6	3386	1.09
S102	200	2	100	60	293	332	1500	6	3682	1.06
S103	150	1	150	25	293	332	1500	6	1873	1.11
S104	150	1	150	43.6	293	332	1500	6	2077	1.13
S105	150	1	150	60	293	332	1500	6	2335	1.15
S106	600	3	200	25	293	332	1500	6	13,513	1.09
S107	600	3	200	43.6	293	332	1500	6	17,092	1.01
S108	600	3	200	60	293	332	1500	6	20,229	0.951
Mean	–	–	–	–	–	–	–	–	–	1.01
COV	–	–	–	–	–	–	–	–	–	0.07

strain) and ultimate strain, respectively. The cross-section slenderness is expressed as:

$$\lambda_c = \sqrt{\frac{\sigma_{0.2}}{\sigma_{cr}}} \tag{7b}$$

$$\sigma_{cr} = \frac{E}{\sqrt{3(1-\nu^2)}}\frac{2t_s}{D_s} \tag{7c}$$

where σ_{cr} is the elastic local critical stress.

The stress-strain relationship of the stainless steel material is idealized to a bi-linear relationship as shown in Fig. 19. The local buckling stress can be calculated using Eqs. (7d)–(7e) [12].

$$\sigma_{LB} = E\varepsilon_{LB}\frac{\varepsilon_{LB}}{\varepsilon_{0.2}} < 1 \tag{7d}$$

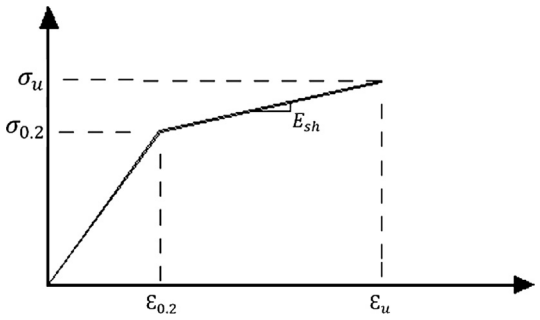

Fig. 19. Bi-linear idealization of Stainless Steel Response.

$$\sigma_{LB} = \sigma_{0.2} + E_{sh}\varepsilon_{0.2}\left(\frac{\varepsilon_{LB}}{\varepsilon_{0.2}} - 1\right)\frac{\varepsilon_{LB}}{\varepsilon_{0.2}} \geq 1 \tag{7e}$$

The axial strength capacity of the concrete infill was defined as:

$$P_{core} = A_c f_{cc} \tag{8}$$

where A_c is the cross-sectional area of the concrete core. The concrete fill is subjected to confinement pressure provided by the CFRP wrap and the stainless steel tube, as illustrated in Fig. 20. Over the past two decades, many investigations have been conducted to understand the behavior of axial compressive FRP-confined concrete. Ozbakkaloglu

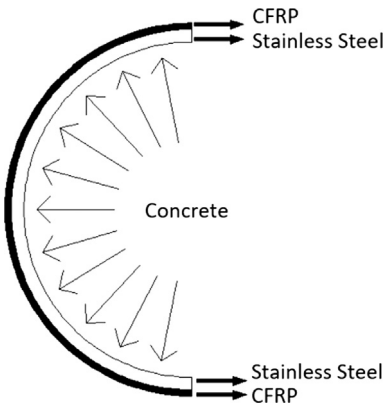

Fig. 20. Confinement pressure provided by the CFRP and the stainless steel.

et al. [59] summarized, classified and evaluated 88 models proposed, in the literature, to predict the behavior of FRP-confined concrete in circular sections. Many of these existing design-oriented models for FRP-confined concrete take the following simple form that was adopted in this study:

$$f_{cc} = f_c + \psi f_l \tag{9}$$

where f_l is the lateral confining pressure and ψ is a confinement parameter that was obtained using the curve fitting for the P_{FE} results obtained from the FEMs. The confining pressure generated by the stainless steel tube and the CFRP wrap can be derived from the force equilibrium of the hoop stresses in these two components, as shown in Fig. 20, to be expressed as:

$$f_l = \frac{2\sigma_\theta t_s}{D_s} + \frac{2f_f t_f}{D_s} \tag{10}$$

where $\sigma_\theta$is the hoop stress in the stainless steel tube where ($\sigma_\theta = 0.1\ \sigma_{0.2}$), f_f is the ultimate tensile strength of the CFRP jacket and t_f is the CFRP jacket thickness. Eq. (9) can then be rewritten in the form shown below.

$$f_{cc} = f_c + \frac{\psi}{D_s}(\sigma_\theta t_s + f_f t_f) \tag{11}$$

Eq. (5) can then be rewritten in the following form.

$$P_u = A_s \sigma_{LB} + A_c\left(f_c + \frac{\psi}{D_s}(\sigma_\theta t_s + f_f t_f)\right) \tag{12}$$

The 108 results of P_{FE} summarized in Table 7 were used to develop a best fit for Eq. (13). The best representation of the ψ parameter was not a constant or linear expression; it was a nonlinear formula. The nonlinear expression shown in Eq. (13) was obtained from a regression analysis.

$$\psi = 7.2 \times \left(\frac{t_s}{D_s}\right)^{0.43} \times \left(\frac{\sigma_{0.2}}{f_c}\right)^{0.3} \times \left(\frac{t_f}{t_s}\right)^{0.08} \tag{13}$$

Eqs. (12) and (13) represent the final proposed model to predict the axial load carrying capacity of CFRP-wrapped CFSST columns. From Table 7, the proposed analytical model provides accurate estimations, where the mean and COV of the ratio P_{FE}/P_u are, respectively, 1.01 and 0.07. A comparison of the load carrying capacity obtained from the FE parametric study and that obtained from the proposed model is shown in Fig. 21.

The variations in the load carrying capacity obtained from the FE analysis, P_{FE}, with the load carrying capacity calculated by the proposed model, P_u, versus D/t, $\sigma_{0.2}/f'_c$ and t_f/t_s ratios are displayed in Fig. 22. From the variations illustrated in Fig. 21, a reduction factor, Ω, of 0.85 should be taken for P_u to make the proposed model conservative. Therefore, Eq. (12) becomes as follows:

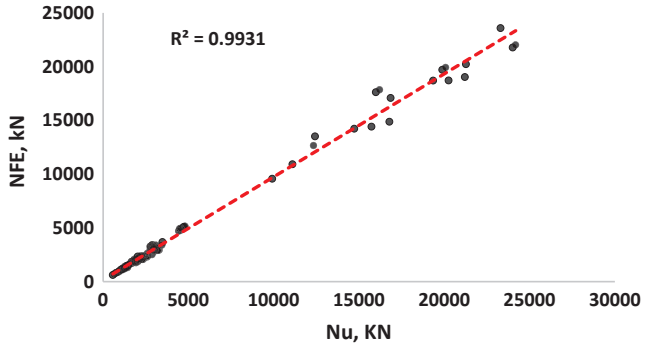

Fig. 21. Comparison of the load carrying capacity obtained from the FE parametric study and the proposed model.

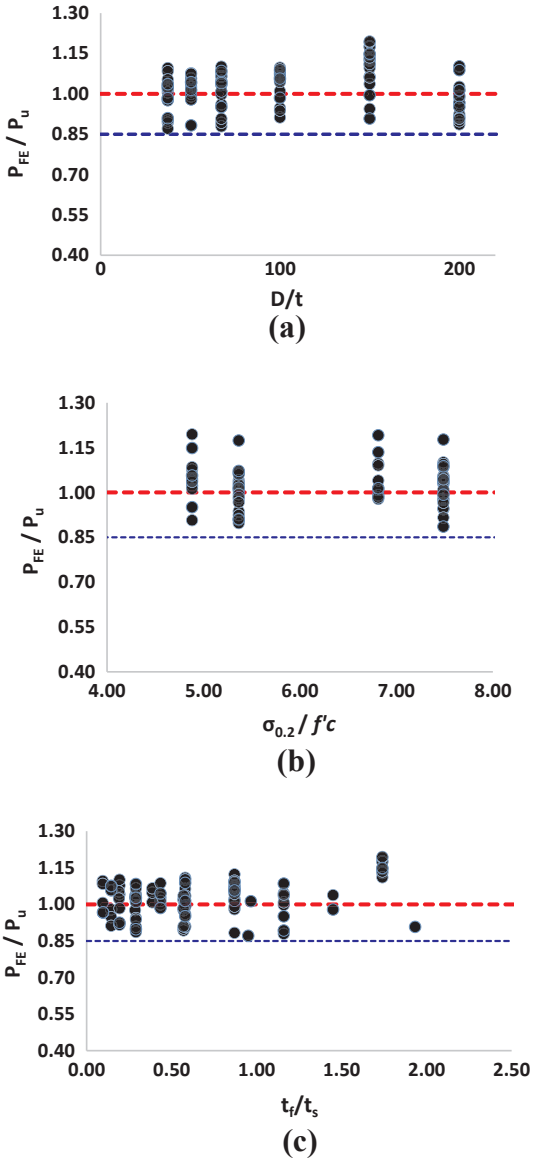

Fig. 22. Variation of P_{FE} to P_u ratio as a function of (a) D/t ratio, (b) $\sigma_{0.2}/f'_c$ ratio and (c) t_f/t_s ratio.

$$\Omega P_u = 0.85[A_s \sigma_{LB} + A_c\left(f_c + \frac{\psi}{D_s}(\sigma_\theta t_s + f_f t_f)\right)] \tag{14}$$

The above-developed equation is limited to predicting the load carrying capacity of CFRP-wrapped CFSST columns. In the case of the CFRP-wrapped CFCST columns, σ_{LB} in Eq. (14) should be replaced by the yielding strength of carbon steel, and the confinement parameter, ψ, should be evaluated from the curve fitting data of the CFRP-wrapped filled carbon steel tubes.

5. Conclusions

Experimental, numerical and analytical investigations were presented in this paper to study the behavior of CFRP-wrapped concrete-filled stainless steel tubes under axial compression. External CFRP wrapping was used to restrain the outward local buckling deformation of the stainless steel tubes, as well as to provide additional confinement to the concrete infill. Based on experimental, numerical and analytical investigations, the following conclusions can be drawn:

CFRP confined CFSST specimens failed because of the rupture of the

CFRP due to the lateral expansion of concrete, however, the non-confined CFSST specimens failed due to excess outward local buckling inelastic deformation near one column end.

Partial wrapping has not shown noticeable improvement in load carrying capacity.

The CFRP jacketing is highly effective in improving the axial compressive behavior of CFSST columns, in terms of the ultimate strength and the axial shortening capacity.

The increase in the CFRP jacket thickness lead to a significant improvement in the ultimate load carrying capacity and the axial shortening capacity.

The FE analysis showed that the CFRP-wrapped CFSST columns were not sensitive to the geometric imperfections.

A large number of results obtained from the FE parametric study for many variables were considered in this study in order to propose an effective model for predicting the load carrying capacity of CFRP wrapped CFSST short columns. The predictions of the proposed model differ from the results of the FE by a coefficient of variation of 0.07 and a standard deviation of 1.01. The difference between the FE results and the results obtained from the proposed model is acceptable.

Acknowledgement

This research work was funded by the Deanship of Scientific Research in King Fahd University of Petroleum and Minerals (KFUPM), Saudi Arabia. Grant No. IN161047.

References

[1] Gardner L, Cruise RB, Sok CP, Krishnan K, Ministro J. Life cycle costing of metallic structures. Proc CE Eng Sust 2007;160:167–77. https://doi.org/10.1680/ensu.2007.160.4.167.
[2] Gardner L. The use of stainless steel in structures. Prog Struct Eng Mater 2005;7:45–55. https://doi.org/10.1002/pse.190.
[3] Rasmussen BKJR, Hancock GJ. Stainless steel structural members. Outline Test Program 2006;119:2349–67.
[4] Young B, Hartono W, Asce M. Compression tests of stainless steel tubular members 2002; 128: 754–61.
[5] Gardner L, Nethercot DA. Experiments on stainless steel hollow sections – Part 1: Material and cross-sectional behaviour. J Constr Steel Res 2004;60:1291–318. https://doi.org/10.1016/j.jcsr.2003.11.006.
[6] Gardner L, Nethercot DA. Experiments on stainless steel hollow sections – Part 2: Member behaviour of columns and beams. J Constr Steel Res 2004;60:1319–32. https://doi.org/10.1016/j.jcsr.2003.11.007.
[7] Gardner L, Nethercot DA. Numerical modeling of stainless steel structural components — a consistent approach 2004; 130: 1586–601.
[8] Gardner L, Ashraf M. Structural design for non-linear metallic materials. Eng Struct 2006;28:926–34. https://doi.org/10.1016/j.engstruct.2005.11.001.
[9] Ashraf M, Gardner L, Nethercot DA. Structural stainless steel design: resistance based on deformation capacity 2008; 134: 402–11.
[10] Afshan S, Gardner L. Experimental study of cold-formed ferritic stainless steel hollow sections. J Struct Eng 2013;139:717–28. https://doi.org/10.1061/(ASCE)ST.1943-541X.0000580.
[11] Ashraf M, Gardner L, Nethercot DA. Compression strength of stainless steel cross-sections. J Constr Steel Res 2006;62:105–15. https://doi.org/10.1016/j.jcsr.2005.04.010.
[12] Buchanan C, Gardner L, Liew A. The continuous strength method for the design of circular hollow sections. J Constr Steel Res 2016;118:207–16. https://doi.org/10.1016/j.jcsr.2015.11.006.
[13] Zhao O, Afshan S, Gardner L. Structural response and continuous strength method design of slender stainless steel cross-sections. Eng Struct 2017;140:14–25. https://doi.org/10.1016/j.engstruct.2017.02.044.
[14] Afshan S, Gardner L. The continuous strength method for structural stainless steel design. Thin-Wall Struct 2013;68:42–9. https://doi.org/10.1016/j.tws.2013.02.011.
[15] Zhao O, Gardner L, Young B. Thin-walled structures structural performance of stainless steel circular hollow sections under combined axial load and bending – Part 1: Experiments and numerical modelling 2016; 101: 231–9.
[16] Zhao O, Rossi B, Gardner L, Young B. Experimental and numerical studies of ferritic stainless steel tubular cross sections under combined compression and bending. J Struct Eng ASCE 2015;142. https://doi.org/10.1061/(ASCE)ST.1943-541X.0001366.
[17] Lam D, Gardner L. Structural design of stainless steel concrete filled columns. J Constr Steel Res 2008;64:1275–82. https://doi.org/10.1016/j.jcsr.2008.04.012.
[18] Schneider S. Axially loaded concrete-filled steel tubes. J Struct Eng ASCE 1998;124:1125–38. https://doi.org/10.1016/j.ijthermalsci.2010.06.009.
[19] Liu D, Gho WM, Yuan J. Ultimate capacity of high-strength rectangular concrete-filled steel hollow section stub columns. J Constr Steel Res 2003;59:1499–515. https://doi.org/10.1016/S0143-974X(03)00106-8.
[20] Giakoumelis G, Lam D. Axial capacity of circular concrete-filled tube columns. J Constr Steel Res 2004;60:1049–68. https://doi.org/10.1016/j.jcsr.2003.10.001.
[21] Faxing D, Lei F, Zhiwu Y, Gang L. Thin-walled structures mechanical performances of concrete-filled steel tubular stub columns with round ends under axial loading 2015; 97: 22–34.
[22] Ding FX, Liu J, Liu XM, Yu ZW, Li DW. Mechanical behavior of circular and square concrete filled steel tube stub columns under local compression. Thin-Wall Struct 2015;94:155–66. https://doi.org/10.1016/j.tws.2015.04.020.
[23] Han LH, Yao GH. Experimental behaviour of thin-walled hollow structural steel (HSS) columns filled with self-consolidating concrete (SCC). Thin-Wall Struct 2004;42:1357–77. https://doi.org/10.1016/j.tws.2004.03.016.
[24] Young B, Ellobody E. Experimental investigation of concrete-filled cold-formed high strength stainless steel tube columns. J Constr Steel Res 2006;62:484–92. https://doi.org/10.1016/j.jcsr.2005.08.004.
[25] Dabaon MA, El-Boghdadi MH, Hassanein MF. Experimental investigation on concrete-filled stainless steel stiffened tubular stub columns. Eng Struct 2009;31:300–7. https://doi.org/10.1016/j.engstruct.2008.08.017.
[26] Uy B, Tao Z, Han LH. Behaviour of short and slender concrete-filled stainless steel tubular columns. J Constr Steel Res 2011;67:360–78. https://doi.org/10.1016/j.jcsr.2010.10.004.
[27] Ellobody E, Ghazy MF. Experimental investigation of eccentrically loaded fibre reinforced concrete-filled stainless steel tubular columns. J Constr Steel Res 2012;76:167–76. https://doi.org/10.1016/j.jcsr.2012.04.001.
[28] Tam VWY, Wang Z-B, Tao Z. Behaviour of recycled aggregate concrete filled stainless steel stub columns. Mater Struct 2014;47:293–310. https://doi.org/10.1617/s11527-013-0061-1.
[29] Patton ML, Singh KD. Finite element modelling of concrete-filled lean duplex stainless steel tubular stub columns. Int J Steel Struct 2014;14:619–32. https://doi.org/10.1007/s13296-014-3020-y.
[30] Tokgoz S. Tests on plain and steel fiber concrete-filled stainless steel tubular columns. J Constr Steel Res 2015;114:129–35. https://doi.org/10.1016/j.jcsr.2015.07.013.
[31] Han LH, Xu CY, Tao Z. Performance of concrete filled stainless steel tubular (CFSST) columns and joints: summary of recent research. J Constr Steel Res 2018. https://doi.org/10.1016/j.jcsr.2018.02.038.
[32] xing Ding F, ren Lu D, Bai Y, zhi Gong Y, wu Yu Z, Ni M, Li W. Behaviour of CFRP-confined concrete-filled circular steel tube stub columns under axial loading. Thin-Wall Struct 2018;125:107–18. https://doi.org/10.1016/j.tws.2018.01.015.
[33] Xiao Y, He W, Choi K. Confined concrete-filled tubular columns 2005; 131: 488–97.
[34] Hu Y, Yu T, Teng J. FRP-confined circular concrete-filled thin steel tubes under axial compression. J Compos Constr 2011;15:850–60. https://doi.org/10.1061/(ASCE)CC.1943-5614.0000217.
[35] Yu T, Hu YM, Teng JG. FRP-confined circular concrete-filled steel tubular columns under cyclic axial compression. J Constr Steel Res 2014;94:33–48. https://doi.org/10.1016/j.jcsr.2013.11.003.
[36] Haedir J, Zhao XL. Design of short CFRP-reinforced steel tubular columns. J Constr Steel Res 2011;67:497–509. https://doi.org/10.1016/j.jcsr.2010.09.005.
[37] Sundarraja MC, Prabhu GG. Experimental study on CFST members strengthened by CFRP composites under compression. J Constr Steel Res 2012;72:75–83. https://doi.org/10.1016/j.jcsr.2011.10.014.
[38] Feng R, Chen Y, Wei J, Huang J, Huang J, He K. Experimental and numerical investigations on flexural behaviour of CFRP reinforced concrete-filled stainless steel CHS tubes. Eng Struct 2018;156:305–21. https://doi.org/10.1016/j.engstruct.2017.11.032.
[39] Dong JF, Wang QY, Guan ZW. Structural behaviour of recycled aggregate concrete filled steel tube columns strengthened by CFRP. Eng Struct 2013;48:532–42. https://doi.org/10.1016/j.engstruct.2012.11.006.
[40] Ganesh Prabhu G, Sundarraja MC, Kim YY. Compressive behavior of circular CFST columns externally reinforced using CFRp composites. Thin-Wall Struct 2015;87:139–48. https://doi.org/10.1016/j.tws.2014.11.005.
[41] ASTM E8/E8M-13. Standard test methods for tension testing of metallic materials. ASTM International, West Conshohocken, PA; 2013. (n.d.).
[42] Ramberg W, Osgood WR. Description of stress–strain curves by three parameters. Technical note no. 902. Washington (DC): National Advisory Committee for Aeronautics; 1943. (n.d.).
[43] Hill HN. Determination of stress–strain relations from offset yield strength values. Technical note no927. Washington (DC): National Advisory Committee for Aeronautics; 1944. (n.d.).
[44] ASTM C39/C39M-18. Standard test method for compressive strength of cylindrical concrete specimens. ASTM International, West Conshohocken, PA; 2018 (n.d.).
[45] ABAQUS. ABAQUS theory and user manuals. Version 6.13-1; 2013. (n.d.).
[46] Hassanein MF. Numerical modelling of concrete-filled lean duplex slender stainless steel tubular stub columns. J Constr Steel Res 2010;66:1057–68. https://doi.org/10.1016/j.jcsr.2010.03.008.
[47] Patel VI, Hassanein MF, Thai HT, Al Abadi H, Paton-Cole V. Behaviour of axially loaded circular concrete-filled bimetallic stainless-carbon steel tubular short columns. Eng Struct 2017;147:583–97. https://doi.org/10.1016/j.engstruct.2017.05.064.
[48] Hassanein MF, Kharoob OF, Liang QQ. Behaviour of circular concrete-filled lean duplex stainless steel-carbon steel tubular short columns. Eng Struct 2013;56:83–94. https://doi.org/10.1016/j.engstruct.2013.04.016.
[49] Hu H-T, Huang C-S, Wu M-H, Wu Y-M. Nonlinear analysis of axially loaded

concrete-filled tube columns with confinement effect. J Struct Eng 2003;129:1322–9. https://doi.org/10.1061/(ASCE)0733-9445(2003).
[50] Mander P, Priestley JB, Park MJN. Theoretical stress-srain model for confined concrete. J Struct Eng 1989;114:1804–26. https://doi.org/10.1061/(ASCE)0733-9445.
[51] ACI. Building code requirements for structural concrete and commentary. ACI 318 M-08. USA: American Concrete Institute; 2008 (n.d.).
[52] Saenz LP. Discussion of 'Equation for the stress–strain curve of concrete' by P. Desayi, and S. Krishnan. ACI J 1964; 61: 1229–35 (n.d.).
[53] Ellobody E, Young B, Lam D. Behaviour of normal and high strength concrete-filled compact steel tube circular stub columns. J Constr Steel Res 2006;62:706–15. https://doi.org/10.1016/j.jcsr.2005.11.002.
[54] Alam MI, Fawzia S, Liu X. Effect of bond length on the behaviour of CFRP strengthened concrete-filled steel tubes under transverse impact. Compos Struct 2015;132:898–914. https://doi.org/10.1016/j.compstruct.2015.06.065.
[55] Hashin Z. Failure criteria for uni-directional fibre composites. J Appl Mech 1980;47(1):329–34.
[56] Hany NF, Hantouche EG, Harajli MH. Finite element modeling of FRP-confined concrete using modified concrete damaged plasticity. Eng Struct 2016;125:1–14. https://doi.org/10.1016/j.engstruct.2016.06.047.
[57] Shi Y, Swait T, Soutis C. Modelling damage evolution in composite laminates subjected to low velocity impact. Compos Struct 2012;94:2902–13. https://doi.org/10.1016/j.compstruct.2012.03.039.
[58] Chang X, Liang Ru Z, Zhou W, Bin Zhang Y. Study on concrete-filled stainless steel-carbon steel tubular (CFSCT) stub columns under compression. Thin-Wall Struct 2013;63:125–33. https://doi.org/10.1016/j.tws.2012.10.002.
[59] Ozbakkaloglu T, Lim JC, Vincent T. FRP-confined concrete in circular sections: review and assessment of stress-strain models. Eng Struct 2013;49:1068–88. https://doi.org/10.1016/j.engstruct.2012.06.010.